Journal of ELECTRONIC MATERIALS, Vol. 49, No. 11, 2020
https://doi.org/10.1007/s11664-020-08195-7
© 2020 The Minerals, Metals & Materials Society

TOPICAL COLLECTION: U.S. WORKSHOP ON PHYSICS AND CHEMISTRY OF II-VI MATERIALS 2019

# Performance Limits of III–V Barrier Detectors

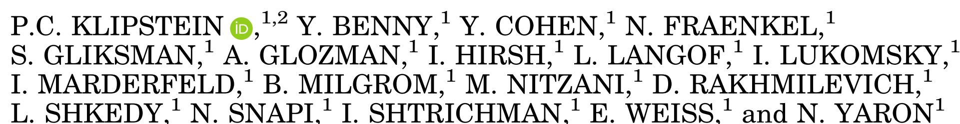
P.C. KLIPSTEIN,[1,2] Y. BENNY,[1] Y. COHEN,[1] N. FRAENKEL,[1] S. GLIKSMAN,[1] A. GLOZMAN,[1] I. HIRSH,[1] L. LANGOF,[1] I. LUKOMSKY,[1] I. MARDERFELD,[1] B. MILGROM,[1] M. NITZANI,[1] D. RAKHMILEVICH,[1] L. SHKEDY,[1] N. SNAPI,[1] I. SHTRICHMAN,[1] E. WEISS,[1] and N. YARON[1]

1.—SemiConductor Devices, P.O. Box 2250, 31021 Haifa, Israel. 2.—e-mail: philip_k@scd.co.il

Minority-carrier lifetimes and diffusion lengths have been deduced from a comparison of band structure simulations and experimental measurements on mid-wave infrared InAsSb XB*n* and long-wave infrared InAs/GaSb type II superlattice (T2SL) XB*p* barrier detectors with low diffusion-limited dark current close to mercury cadmium telluride Rule 07 and high quantum efficiency. For the XB*n* devices, a lifetime of 1.9 $\mu$s was observed with a corresponding diffusion length of 14.5 $\mu$m. In contrast, the T2SL exhibited a much shorter lifetime of 7.5 ns, but the diffusion length of $\sim$ 7 $\mu$m was long enough to ensure that almost 90% of the photocarriers are collected. The lifetime appears to be Auger limited in the case of *n*-type InAsSb, but for the *p*-type T2SL, Shockley–Read–Hall (SRH) traps appear to dominate. In the second case, possible scenarios for the dominance of SRH recombination are discussed to identify pathways for further performance optimization.

**Key words:** Infrared detector, barrier detector, InAsSb, type II superlattice, Auger, Shockley–Read–Hall

## INTRODUCTION

Group III–V semiconductor materials offer unique possibilities for band structure engineering. The InAs/InSb/GaSb/AlSb family of alloys and superlattice materials can be grown with high quality on GaSb or InSb substrates with satisfactory control of strain, doping, and composition. The band profiles and oscillator strengths are also quite predictable, enabling full simulation of detector performance from a basic knowledge of layer and stack thicknesses. These characteristics have recently stimulated a major worldwide effort aimed at developing III–V infrared detectors with performance comparable to but cost lower than traditional II–VI devices.

In conventional III–V *p*–*n* devices, Shockley–Read–Hall (SRH) traps result in a significant flow of thermally generated carriers in the device depletion region. At SemiConductor Devices (SCD), we have developed III–V barrier device architectures that can suppress this dark current, leading to higher operating temperatures. These architectures are known generically as XB*n* and XB*p* structures, based on the symbol convention defined in the caption to Fig. 1. The InAsSb XB*n* family of barrier detectors (Fig. 1) operate at 150 K with a cutoff wavelength of 4.2 $\mu$m and background-limited performance (BLIP) up to 175 K at F/3.[1–4] The InAs/GaSb superlattice XB*p* barrier detector (Fig. 2) operates at 77 K with a cutoff near 9.5 $\mu$m and BLIP up to $\sim$ 90 K.[1,2,4] By careful optimization of the passivation and other steps of the focal-plane array (FPA) fabrication process, FPA pixel operabilities at F/3, based on stringent production-line criteria, are typically in excess of 99.5% in all cases.[5,6] Since these devices operate close to the theoretical diffusion limit, it is possible to determine the minority-carrier diffusion length and lifetime from relatively simple measurements on the devices

(Received January 21, 2020; accepted April 29, 2020; published online May 20, 2020)

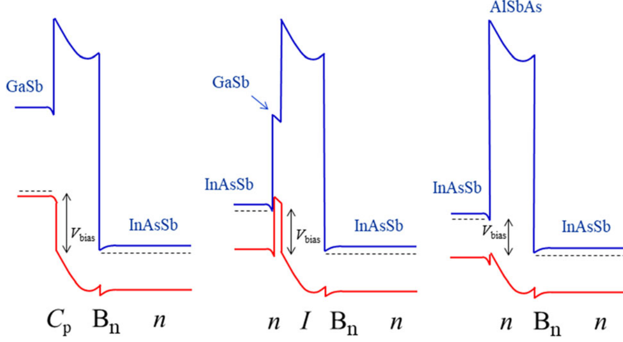


Fig. 1. Schematic band-edge profiles at operating bias for the XB$n$ family of barrier detectors based on an InAsSb absorbing layer lattice matched to a GaSb buffer layer or substrate. In the names written under each device, $C$, $B$ and $I$ stand for "contact," "barrier," and "intermediate" layers respectively, and the subscripts to $n$- or $p$-doping. The final letter in each name represents the $n$-type active layer. If the same symbol appears also as the first letter, it means that the contact and active layers are made from the same $n$-type material.

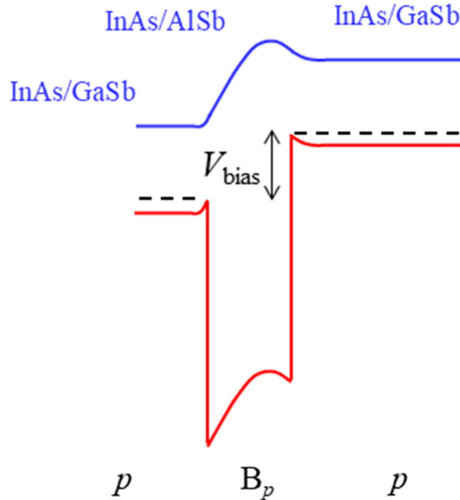


Fig. 2. Schematic band-edge profiles at operating bias for an XB$p$ barrier detector based on an InAs/GaSb T2SL absorbing layer lattice matched to a GaSb substrate. The naming convention is analogous to that used in Fig. 1.

themselves, as a function of sample dimensions and temperature.[7]

The XB$n$ architectures shown in Fig. 1 are all based on the same InAsSb active layer (AL) and AlSbAs barrier layer (BL) materials, both $n$-type and closely lattice matched to a GaSb substrate or buffer layer. For large pitches, pixels may be isolated in all cases by a shallow mesa etch to the top of the BL, while for small pitches a deeper etch is required in order to minimize electrical crosstalk. The main difference between the architectures lies in the design of the contact layer (CL): the $C_pB_nn$ detector has a $p$-type GaSb CL, the $nB_nn$ detector has an $n$-type InAsSb CL, and the $nIB_nn$ detector has a combination of the two, where a thin GaSb intermediate layer is inserted between the BL and an $n$-type InAsSb CL. The main effect of these variations is to change the device operating bias, which is related to the different band offsets. The $C_pB_nn$ and $nIB_nn$ detectors also offer the advantage of avoiding any charge build-up in the BL, which could be a potential source of noise, since they present no blockage to minority carriers passing into the CL.[3]

## LIFETIME

In both the XB$n$ and XB$p$ architectures, the use of the same doping polarity for AL and BL confines all of the depletion region to the wide-bandgap BL, thereby providing good isolation between pixels, even when a shallow etch is used, and suppressing the generation–recombination contribution to the dark current. This suppression leads to very low diffusion-limited dark current density, $J_{\text{diff}} = ep_{n0}L_{\text{AL}}/\tau_{\text{min}}$, where $p_{n0}$ is the minority-carrier concentration, given for low doping levels by $p_{n0} = n_{\text{i}}^2/N_{\text{dop}}$, where $N_{\text{dop}}$ and $L_{\text{AL}}$ are the AL doping and thickness, $n_{\text{i}}$ is the intrinsic carrier concentration, and $\tau_{\text{min}}$ is the minority-carrier lifetime. Using a form of $8 \times 8$ $\mathbf{k}{\cdot}\mathbf{p}$ band theory adapted for narrow-bandgap systems,[8,9] we can determine the conduction- and valence-band dispersions fairly accurately, thus enabling accurate computation of the intrinsic carrier concentration.

For $InAs_{1-x}Sb_x$, the heavy hole (HH) Fermi surface is almost cubic. The HH density of states is given by the standard expression,[10] using an effective mass of $m_{\text{DOS}}^{\text{HH}} \approx (6/\pi)^{\frac{2}{3}} m_{001}^{\text{HH}}$, in which $m_{001}^{\text{HH}} = m_0/(\gamma_1 - 2\gamma_2)$ is the effective mass along [001], $m_0$ is the free electron mass, and $\gamma_1$ and $\gamma_2$ are Luttinger parameters. The light hole (LH) dispersion is essentially isotropic, and its contribution is calculated with an effective mass of $m_{\text{DOS}}^{\text{LH}} \approx m_{001}^{\text{LH}} = m_0/(\gamma_1 + 2\gamma_2)$. The Luttinger parameters are determined using the method described in Ref. 9, which takes the strong band bowing into account, resulting in valence-band mass values of $m_{\text{DOS}}^{\text{HH}} \approx 0.570 m_0$ and $m_{\text{DOS}}^{\text{LH}} \approx 0.021 m_0$, respectively. For the conduction band, which is also isotropic, the effective mass taking band bowing into account[9] is $m_{\text{DOS}}^{E} \approx 0.017 m_0$. The intrinsic carrier concentration can thus be expressed in terms of the masses and the bandgap, $E_{\text{G}}(T)$, as $n_{\text{i}} = 2/h^3 (m_{\text{DOS}}^{\text{E}})^{\frac{3}{4}} \left\{ (m_{\text{DOS}}^{\text{HH}})^{\frac{3}{2}} + (m_{\text{DOS}}^{\text{LH}})^{\frac{3}{2}} \right\}^{\frac{1}{2}} (2\pi kT)^{\frac{3}{2}} \exp(-E_{\text{G}}/2kT)$. For the type II superlattice (T2SL), the dispersion is rather more complicated, and it is therefore better to calculate the intrinsic carrier concentration directly from the $\mathbf{k}{\cdot}\mathbf{p}$ band dispersions, as described in Ref. 7.

$N_{\text{dop}}$ is found from the bias dependence of the device capacitance, as shown in Ref. 7. The lifetime $\tau_{\text{min}}$ can thus be determined by fitting the calculated curve for $J_{\text{diff}}(T)$ to the experimentally measured dark current density. The points in Fig. 3 are the bulk dark current density for an InAsSb XB$n$ device

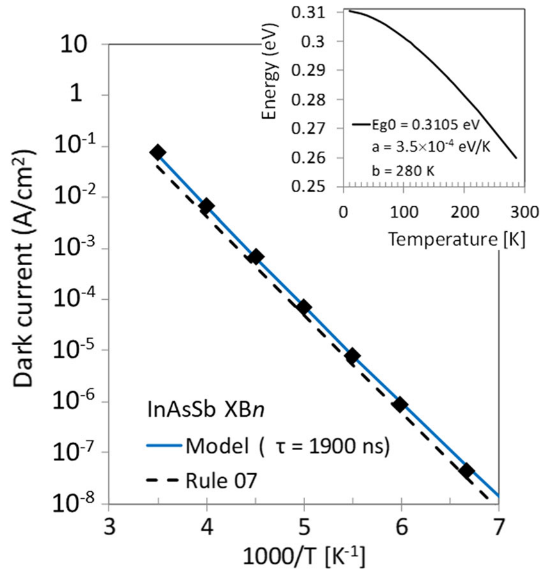


Fig. 3. Plot of logarithm of dark current versus reciprocal temperature for an XB$n$ device with AL doping of $6.5 \times 10^{15}$ cm$^{-3}$ (points) and fit to a **k·p** model with a lifetime of 1900 ns (solid line). The Rule 07 dependence is shown as a dashed line. The fit is based on a Varshni formulation of the bandgap that agrees with experiment,[11] as plotted in the inset together with the Varshni parameters.

with an AL width of 3.5 $\mu$m and doping of $n = 6.5 \times 10^{15}$ cm$^{-3}$. Any perimeter effects, for example, due to lateral diffusion from regions outside the mesa, have been excluded based on measurements on mesas of different sizes, as described in Ref. 7. An excellent fit is shown with a hole lifetime of $\tau_{\rm min} = \tau_{\rm p} = 1.9$ $\mu$s. Note that, although the LH was included, its contribution is found to be quite negligible. We used a bandgap variation with temperature based on the results in Ref. 11, which fit very well to the Varshni curve[12] shown in the inset of Fig. 3. This corresponds to a bandgap wavelength of 4.24 $\mu$m at the detector operating temperature of 150 K, which is almost a perfect match to the long-wavelength edge of the upper, highly transparent, mid-wave infrared (MWIR) atmospheric window. Also plotted, as a dashed line in Fig. 3, is the dark current density according to mercury cadmium telluride (MCT) Rule 07,[13] which can be seen to be very close to that of the XB$n$ device. A fit to the dark current density for another device with a much higher AL doping of $n = 1.5 \times 10^{17}$ cm$^{-3}$ was found to yield $\tau_{\rm min} = 4$ ns. In this case there is significant Moss–Burstein (MB) filling of the conduction band, with a filling energy of $E_{\rm MB} = 52$ meV as determined from the **k·p** formula given in Ref. 14. The minority-carrier concentration must then be calculated as $p_{n0} = 2/h^3\left\{\left(m_{\rm DOS}^{\rm HH}\right)^{\frac{3}{2}} + \left(m_{\rm DOS}^{\rm LH}\right)^{\frac{3}{2}}\right\}(2\pi kT)^{\frac{3}{2}}$ $\exp[-(E_{\rm G}(T) + E_{\rm MB})/kT]$, although again the LH contribution is quite negligible. For both doping levels, the minority hole lifetimes obey a variation of the form $\tau_p(ns) = 3.09 \times 10^{33} n^{-1.92}$, which is close to the inverse quadratic behavior expected for Auger recombination.* In spite of the short lifetime, the dark current density in the highly doped sample is only a factor of 2–3 above the Rule 07 value.[13] This is because the MB effect increases the effective bandgap by about 17%. The MB effect was taken into account in the fit to the dark current density but not for Rule 07. MB effects are undesirable since they block the long-wavelength absorption and reduce the overall quantum efficiency (QE).[15]

Figure 4 shows the bulk dark current density for a long-wave infrared (LWIR) XB$p$ device with a 4.5-$\mu$m-thick T2SL absorber and the bandgap variation shown in the inset. The cutoff wavelength at 77 K is 9.8 $\mu$m. In this case the fit lifetime is $\tau_{\rm min} = 7.5$ ns, which is much shorter than for an XB$n$ device with similar doping ($\sim 10^{16}$ cm$^{-3}$). Nevertheless, the dark current density is only about ten times the Rule 07 value. This appears to be because the lifetime is only weakly dependent on the $p$-doping level of the AL, and the Moss–Burstein effect is much weaker for holes, so relatively high doping can be used.[15]

## DIFFUSION LENGTH

Lateral diffusion lengths, $L_{\|}$, at the MWIR XB$n$ operating temperature of 150 K can be estimated from the size dependence of the dark current or QE, based on the method discussed in Ref. 7. Measurements of the average QE were performed in the wavelength range from 3.2 $\mu$m to 3.6 $\mu$m and fit to the formula ${\rm QE} = {\rm QE}_\infty\left[\left(L + 2L_{\|}\right)^2 / L^2\right]$, where $L$ is the side dimension of the square mesa as shown in the inset to Fig. 5a. A lateral diffusion length of $L_{\|} = 14.5$ $\mu$m was obtained for a reference sample grown on a GaSb substrate, which had a 3-$\mu$m-thick AL but was otherwise nominally identical to the sample used in Fig. 3. This value can also be taken as a minimum value for the vertical diffusion length, $L_{\perp}$, along the growth direction, since a nonzero surface recombination velocity would only reduce $L_{\|}$. Values of $L_{\|}$ are plotted in Fig. 5a versus the full-width at half-maximum (FWHM) of the double-axis x-ray diffraction peak obtained from the InAsSb AL, for the reference sample and for similar devices grown at the same time on GaAs substrates with different GaSb buffer widths. For thinner buffer widths, the crystalline quality of the InAsSb AL is lower, so the FWHM is larger. As can be seen from this figure, a FWHM of $\sim$ 100 s or smaller is

*In Ref. 15, a variation of the form $\tau_p \propto n^{-1.3}$ was plotted and taken as evidence for a more linear variation as expected for a Shockley–Read–Hall recombination mechanism. However, the plot included samples from more than one molecular beam epitaxy (MBE) machine, and the determination of the density of states was not as accurate as described herein. In any case, more points are required for samples grown in the same MBE machine with different carrier concentrations to improve the fitting of the $n$-dependence.

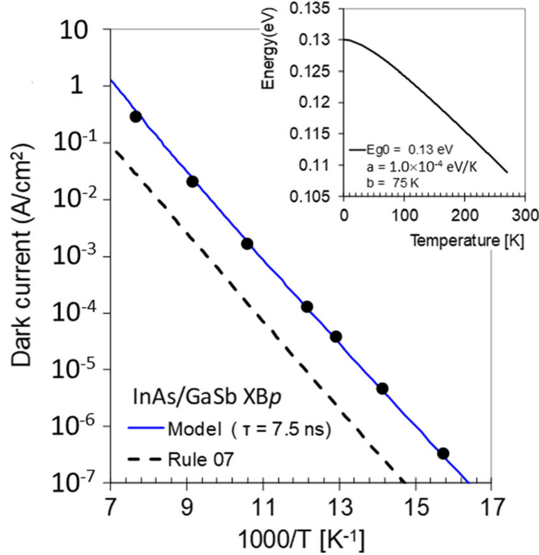


Fig. 4. The points show dark current results for an XB*p* device with the bandgap energy variation with temperature shown in the inset (bandgap wavelength at 77 K = 9.8 $\mu$m). The corresponding fit with a minority electron lifetime of 7.5 ns is shown as a solid line. Rule 07 is shown for comparison as a dashed line.

necessary to reach parity with the reference sample, which, as previously reported, can be achieved for buffer widths of several microns.[16] Growth on GaAs allows the use of a larger substrate than is possible with GaSb, with the potential to reduce manufacturing costs quite significantly.

Figure 5b shows a simulation of the QE at a wavelength of 3.4 $\mu$m, normalized to its value for an infinite vertical diffusion length, $L_{\perp}$, as a function of the length ratio, $L_{\perp}/L_{\mathrm{AL}}$. The simulation is based on the optical transfer matrix technique and a semiempirical formula for the absorption coefficient, which have been shown previously to match experiment fairly well.[15] The simulation shows that, for $L_{\perp}/L_{\mathrm{AL}} > 4$, corresponding to both the thickest buffer and the reference sample, more than 95% of the absorbed radiation is converted to a signal. For these samples, $\mathrm{QE}_{\infty}$ was 53% with no antireflection coating (ARC), corresponding to an external QE of 76% with ARC.

In Fig. 6, the size dependence of the average QE measured at 77 K in the wavelength range from 7.9 $\mu$m to the sample cutoff wavelength of 9.8 $\mu$m is shown as points for LWIR XB*p* devices on the same test chip as used for the dark current measurements in Fig. 4. A fit, as described above, is shown as a solid line, yielding $\mathrm{QE}_{\infty}$ = 45% and $L_{\parallel}$ = 6.6 $\mu$m. These devices are two-pass devices with an optically reflective metal contact that occupies almost all of the upper surface of the CL (i.e., metal fill factor, FF = 1). Since it was shown in the previous section that the lifetime is very short, it is probably reasonable to assume that, in contrast to the XB*n* device, the lateral diffusion length in the T2SL is relatively unaffected by any surface recombination. By adding an ARC, the value of $\mathrm{QE}_{\infty}$ should increase to 64%. A

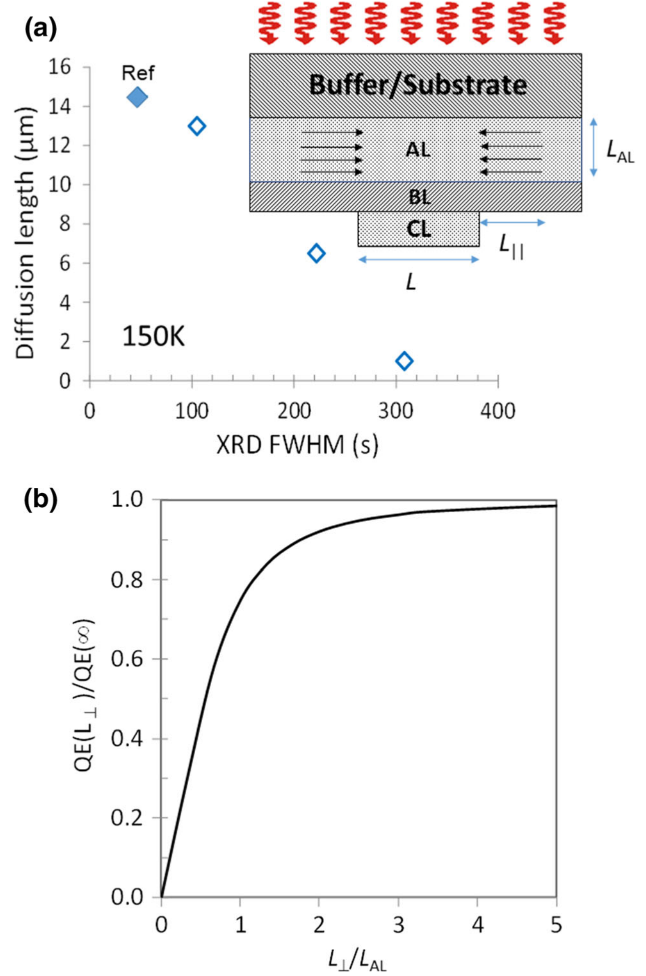


Fig. 5. (a) Lateral diffusion length deduced from measurements of the size dependence of the QE at 150 K as a function of mesa dimension versus FWHM of the double-axis x-ray diffraction line, for the XB*n* samples grown on GaAs substrates and for the reference sample. Inset shows lateral diffusion of minority carriers from outside the mesa area, with a diffusion length, $L_{\parallel}$. (b) Simulation of the average QE as a function of vertical diffusion length, $L_{\perp}$.

simulation of the average QE, in which the vertical diffusion length, $L_{\perp}$, is adjusted until the QE value matches that of $\mathrm{QE}_{\infty}$, shows that the vertical diffusion length has a similar value to the lateral one, so that $L_{\perp}/L_{\mathrm{AL}} \approx 1.5$. As shown in the simulation displayed in the inset of Fig. 6, this corresponds to a collection efficiency for photocarriers of nearly 90%. Thus, for both MWIR InAsSb XB*n* and LWIR T2SL XB*p* devices, the diffusion lengths are large enough to ensure high performance with minimal losses in all cases. The short lifetime in the LWIR XB*p* device does not appear to be a severe limitation, thanks to the small electron effective mass, $m_{\mathrm{e}}^{*}$ $0.022m_0$, in the T2SL conduction band.[7]

## LIFETIME MECHANISM IN *P*-TYPE T2SL

The short lifetime in the *p*-type T2SL is generally thought to be related to SRH traps[17] rather than to Auger processes that dominate the lifetime in

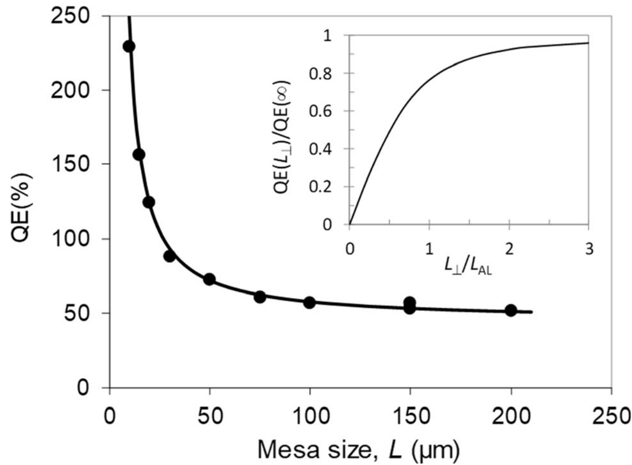


Fig. 6. Size dependence of the average QE at 77 K in the wavelength range from 7.9 $\mu$m to the cutoff wavelength of 9.8 $\mu$m for the XB$p$ device of Fig. 4 (points), and corresponding fit (line) with the parameters given in the text. The device has an optically reflecting contact but no ARC. The inset shows a simulation of the average QE as a function of $L_\perp$.

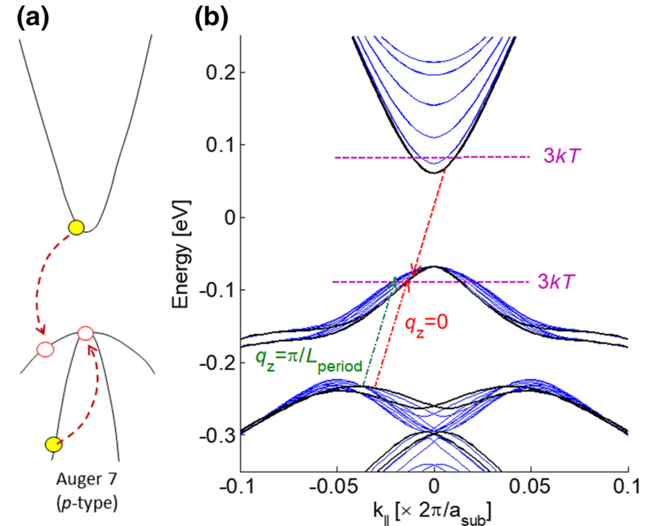


Fig. 7. (a) Schematic of A7 recombination process in bulk $p$-type semiconductor where electrons are shown as yellow dots and holes as red circles. (b) Corresponding A7 process for an $InAs_{14}GaSb_8$ T2SL with a bandgap wavelength of 9.65 $\mu$m, indicated on the in-plane dispersion along [100] calculated with the 8 × 8 **k·p** model described in the text and where $a_{sub}$ is the lattice parameter of the GaSb substrate. The black (blue) curves are for equally spaced values of the wavevector, $q_z$, along the [001] growth direction with $q_z = 0$ ($q_z \neq 0$). The horizontal dashed lines indicate energies of $3kT$ above or below the band edges at 77 K. A7 transitions at $q_z = 0$ ($q_z = \pi/L_{period}$) are shown as dashed lines in red (green), where $L_{period}$ is the T2SL period (Color figure online).

mercury cadmium telluride.[18] It was shown in Ref. 18 that the Auger 7 process, which is usually dominant in bulk $p$-type MCT and which involves both heavy and light holes (Fig. 7a), can be suppressed strongly in the T2SL when the splitting between the relatively flat HH and LH subbands exceeds the T2SL bandgap. The suppression mechanism should thus be most effective in very long-wavelength (VLWIR) T2SLs, which have a small bandgap. This seems to agree with a more recent theoretical analysis[19] where the suppression relative to MCT is strongest for VLWIR (factor of ~ 20 at 15 $\mu$m and 100 K) but more moderate for LWIR and MWIR (factor of ~ 3 at 10.9 $\mu$m and 100 K and ~ 1 at 4.3 $\mu$m and 100 K). Recently, one of the current authors developed an eight-band **k·p** model adapted to narrow-bandgap superlattices that can reproduce experimental LWIR and MWIR T2SL absorption spectra very well. The calculated subband dispersions should therefore be fairly accurate, and an example of the band structure for a $InAs_{14}GaSb_8$ T2SL with a cutoff wavelength of 9.65 $\mu$m is shown in Fig. 7b. For this band structure, Auger 7 transitions are marked where the initial electron and hole states are within $3kT$ of the band edges at $T$ = 77 K, suggesting that the A7 recombination process should in fact be quite effective. Since many larger energy transitions between the valence subbands can also be identified, this should persist to T2SLs with larger energy bandgaps. Nevertheless, the T2SL minority-carrier lifetime does not appear to be very sensitive to doping,[15,20] suggesting that A7 recombination is not the primary cause of recombination and that SRH traps still dominate. Since lifetimes can be much longer in gallium-free InAs/InAsSb T2SLs, there is wide consensus that the important SRH traps are located in the GaSb layers of the InAs/GaSb T2SL.[17,21] It is notable that, in related materials such as vacancy-doped $p$-type HgCdTe where the trap density is proportional to the doping, SRH lifetimes of ~ 400 ns are reported[22] for $p = 10^{15}$ cm$^{-3}$, being much longer than those reported for $p$-type T2SL samples with a similar doping level. Therefore, either the traps in GaSb are due to some natural stoichiometric defect, which is present in unusually high concentrations, or the trap itself acts very efficiently and suppresses competing A7 processes, as depicted in Fig. 8b.

Figure 8 contrasts the recombination processes that can occur when the trap is (a) acceptor like (charged when occupied) or (b) donor like (charged when unoccupied). For the acceptor-like trap depicted in Fig. 8a, the empty trap is neutral so SRH recombination of the minority electron, as represented by the dashed arrows, should be relatively slow.[23] In addition, good overlap should exist between extended electron and hole states near the band edges, promoting the strong electron–hole interactions required for the A7 process, as depicted by the solid arrows. Thus, Auger processes should dominate at relatively low carrier concentrations. In contrast, for a donor-like trap as in Fig. 8b, the positive charge of the empty trap attracts and localizes the minority electron, leading to a short SRH lifetime and repelling holes away from the trap region. The localization of the electron and its poor overlap with the holes will lead to suppression of the A7 process. Instead, the dipole field of the localized state should provide a strong Fröhlich interaction

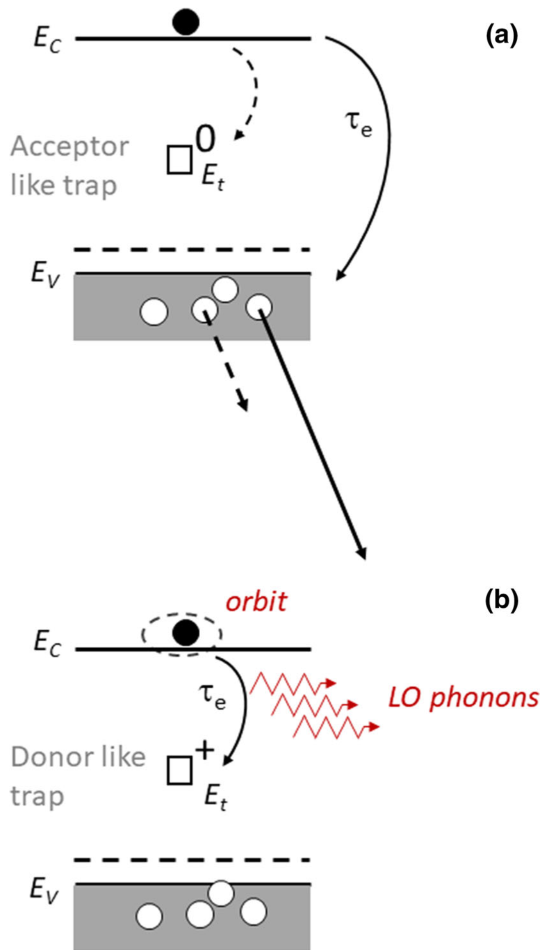


Fig. 8. Schematic diagram of recombination processes in the presence of an SRH trap which is (a) acceptor like and (b) donor like. Note that energy is absorbed in an Auger 7 process in (a) by exciting a hole deeper into the valence band, which is equivalent to exciting a valence-band electron to higher energies in Fig. 7. Energy may also be absorbed in this way (or otherwise) for the SRH process depicted by the dashed arrows.[23] In (b), the positive charge of the empty SRH trap localizes the minority electron in an orbit and repels the majority holes, thereby reducing electron–hole overlap and suppressing the A7 process. This does not occur in (a) because the empty trap is neutral. $E_C$ and $E_V$ are the energies of the conduction- and valence-band edges, and the dashed line is the Fermi level.

with polar optical phonons, which can provide an efficient means of energy relaxation to the SRH state. The increase of the minority-carrier lifetime from 30 ns to 140 ns reported by Connelly et al. in a *p*-type LWIR T2SL when exposed to strong sub-bandgap illumination[17] is consistent with this model. The sub-bandgap absorption will excite electrons from the valence band into the donor-like trap states, rendering them neutral. SRH-based recombination would then be reduced, while the strength of A7 processes would be restored.

## CONCLUSIONS

Barrier devices based on III–V materials, with unipolar doping of the active and barrier layers, can provide low, diffusion-limited, dark currents and high quantum efficiencies close to state of the art. Their band profiles, densities of states, and oscillator strengths can be calculated with a high degree of precision, allowing fundamental parameters such as the minority-carrier lifetime and diffusion length to be deduced from a comparison between simulation and experiment. InAsSb-based MWIR XB*n* detectors with a 4.2-$\mu$m bandgap wavelength grown on GaSb substrates, or on GaAs substrates with a GaSb buffer width of several microns, exhibit Rule 07 performance which can be attributed to a long minority-carrier lifetime and a diffusion length in excess of 10 $\mu$m. A comparison of devices with high and low doping in the AL is consistent with Auger-limited recombination for *n*-doping in excess of $6 \times 10^{15}$ cm$^{-3}$. High doping should be avoided, however, due to strong Moss–Burstein effects, which block the absorption and reduce the lifetime and diffusion length. For InAs/GaSb T2SL XB*p* devices with a bandgap wavelength of 9.8 $\mu$m, the lifetime is very short (7.5 ns) and relatively independent of doping. The dark current is only about ten times the Rule 07 value, while the QE is above 60% for a two-pass device with a 4.5-$\mu$m AL, a metal FF of unity, and an ARC. Note, however, that in a pixel of a focal-plane array detector, the metal FF is smaller, so in this case a slightly lower QE is obtained.[7] A diffusion length of $\sim$ 7 $\mu$m was determined both parallel and perpendicular to the layers, resulting in the collection of nearly 90% of all photocarriers. Even though the electron lifetime is very short, the relatively long diffusion length can be attributed to a very small effective mass near the edge of the conduction miniband. Analysis of the band structure of a LWIR T2SL with a bandgap wavelength of 9.65 $\mu$m, calculated using an eight-band $\mathbf{k}\cdot\mathbf{p}$ model adapted for narrow-bandgap heterostructures, shows that Auger 7 transitions can occur with initial electron and hole states close to the band edges, so the dominance of SRH recombination in the T2SL is intriguing. While this dominance might simply be due to an unusually high concentration of SRH traps in the GaSb layers, a mechanism has also been proposed where a low concentration of donor-like traps can lead to rapid SRH recombination and suppression of A7 processes. Donor passivation by codoping with a suitable passivation species might thus provide a route to increasing the minority lifetime in *p*-type T2SLs.

In summary, although there is room for some further optimization of the T2SL, both MWIR InAsSb XB*n* and LWIR T2SL XB*p* III–V barrier devices exhibit high quantum efficiencies and are already quite close to MCT Rule 07 performance. This, combined with their stability and ease of fabrication, make such barrier devices very attractive as detectors based on alternative materials to MCT.

## ACKNOWLEDGMENTS

The authors acknowledge technical support from Mr. S. Greenberg, who was responsible for the smooth operation of the MBE machine, and Ms. H Schanzer, Mr. Hanan Geva, Ms. H. Moshe, Mr. Y. Caracenti, Ms. N. Hazan, Mr. I. Bogoslavski, Mr. Y. Osmo, Ms. L Krivolapov, and Ms. M. Menahem who all contributed to the successful processing, packaging, or characterization of the materials and devices. We are grateful to Mr. Y. Livneh for computational assistance with the **k·p** simulations.

## REFERENCES

1. P.C. Klipstein, *Depletionless Photodiode with Suppressed Dark Current*, US Patent 7,795,640 (2003).
2. P.C. Klipstein, *Unipolar Semiconductor Photodetector with* …, US Patent 8,004,012 (2006).
3. P.C. Klipstein, *Semiconductor Barrier Photodetector,* US Patent 9,627,563 (22 April 2013).
4. P.C. Klipstein, *Proc. SPIE* 6940, 6940-2U (2008).
5. G. Gershon, E. Avnon, M. Brumer, W. Freiman, Y. Karni, T. Niderman, O. Ofer, T. Rosenstock, D. Seref, N. Shiloah, L. Shkedy, R. Tessler, and I. Shtrichman, *Proc. SPIE* 10177, 10177-1I (2017).
6. P.C. Klipstein, E. Avnon, Y. Benny, Y. Cohen, R. Fraenkel, S. Gliksman, A. Glozman, E. Hojman, O. Klin, L. Krasovitsky, L. Langof, I. Lukomsky, I. Marderfeld, N. Yaron, M. Nitzani, N. Rappaport, I. Shtrichman, N. Snapi, and E. Weiss, *J. Electron. Mater.* 47, 5725 (2018).
7. P.C. Klipstein, Y. Benny, S. Gliksman, A. Glozman, E. Hojman, O. Klin, L. Langof, I. Lukomsky, I. Marderfeld, M. Nitzani, N. Snapi, and E. Weiss, *IR Phys. Technol.* 96, 155 (2019).
8. Y.Livneh, P.C. Klipstein, O. Klin, N. Snapi, S. Grossman, A. Glozman, and E. Weiss, Phys. Rev. B **86**, 235311 (2012); Erratum, Phys. Rev. B **90**, 039903 (2014).
9. P.C. Klipstein, *J. Electron. Mater.* 43, 2984 (2014).
10. D.A. Fraser, *The Physics of Semiconductor Devices*, 4th ed. (Oxford: Clarendon, 1986).
11. M.A. Marciniak, R.L. Hengehold, and Y.K. Yeo, *J. Appl. Phys.* 84, 480 (1998).
12. Y.P. Varshni, *Physica* 34, 149 (1967).
13. W.E. Tennant, *J. Electron. Mater.* 39, 1030 (2010).
14. P.C. Klipstein, O. Klin, S. Grossman, N. Snapi, B. Yaakobovitz, M. Brumer, I. Lukomsky, D. Aronov, M. Yassen, B. Yofis, A. Glozman, T. Fishman, E. Berkowicz, O. Magen, I. Shtrichman, and E. Weiss, *Proc. SPIE* 7608, 7608-1V (2010).
15. P.C. Klipstein, *III–V Semiconductors for Infrared Detectors, Molecular Beam Epitaxy: Materials and Device Applications*, ed. H. Asahi and Y. Horikoshi (Hoboken: Wiley, 2019).
16. E. Weiss, O. Klin, S. Grossmann, N. Snapi, I. Lukomsky, D. Aronov, M. Yassen, E. Berkowicz, A. Glozman, P. Klipstein, A. Fraenkel, and I. Shtrichman, *J. Cryst. Growth* 339, 31 (2012).
17. B.C. Connelly, G.D. Metcalf, H. Shen, and M. Wraback, *Proc. SPIE* 8704, 8704-0V (2013).
18. C.H. Grein, P.M. Young, and E. Ehrenreich, *Appl. Phys. Lett.* 61, 2905 (1992).
19. C.H. Grein, J. Garland, and M.E. Flatte, *J. Electron. Mater.* 38, 1800 (2009).
20. S. Bandara, P. Maloney, N. Baril, J. Pellegrino, and M. Tidrow, *Opt. Eng.* 50, 061015 (2011).
21. E.H. Steenbergen, B.C. Connelly, G.D. Metcalfe, H. Shen, M. Wraback, D. Lubyshev, Y. Qiu, J.M. Fastenau, A.W.K. Liu, S. Elhamri, O.O. Cellek, and Y.H. Zhang, *Appl. Phys. Lett.* 99, 251110 (2011).
22. M.A. Kinch, F. Aqariden, D. Chandra, P.-K. Liao, H.F. Schaake, and H.D. Shih, *J. Electron. Mater.* 34, 880 (2005).
23. M.Y. Pines and O.M. Staffsud, *Infrared Phys.* 20, 73 (1980).

**Publisher's Note** Springer Nature remains neutral with regard to jurisdictional claims in published maps and institutional affiliations.